



---

# **Description of CTA Instrument Response Functions (Production 3b Simulation)**

---

**Authors:**

G.Maier (DESY), J. Bregeon (LUPM), P.Cumani (IFAE), K.Bernlöhr (MPIK), T. Hassan (IFAE), A.Moralejo (IFAE)

**Keywords:**

Analysis, Simulations

**Version History:**

| Ver. | Date       | Comment                              | Distribution | Corresponding... |
|------|------------|--------------------------------------|--------------|------------------|
| 0.1  | 2017-04-19 | early draft                          | CTA internal |                  |
| 0.3  | 2017-05-03 | draft after feedback from co-authors | CTA internal |                  |
| 0.4  | 2017-05-11 | feedback from A.D'Ai                 | CTA internal |                  |
| 0.5  | 2017-05-29 | feedback from J.Rico                 | CTA internal |                  |
| 1.0  | 2017-06-02 | first release                        |              |                  |

# Table of Contents

|          |  |           |
|----------|--|-----------|
| <b>1</b> | <b>Introduction</b>  | <b>4</b>  |
| <b>2</b> | <b>Generation of Instrument Response Function for CTA</b>    | <b>4</b>  |
| 2.1      | Monte Carlo Simulations . . . . .                            | 4         |
| 2.2      | Event Reconstruction and Analysis . . . . .                  | 6         |
| 2.3      | Computing . . . . .  | 6         |
| 2.4      | Sites and Array Layouts . . . . .                            | 7         |
| <b>3</b> | <b>Description of Instrument Response Functions for CTA</b>  | <b>10</b> |
| 3.1      | Definition of variables . . . . .                            | 10        |
| 3.2      | General remarks on IRF histograms . . . . .                  | 10        |
| 3.3      | Point-source direction ( $\Theta^2$ ) cut . . . . .          | 11        |
| 3.4      | Collection Area . . . . .                                    | 11        |
| 3.5      | Spacial resolution function and angular resolution . . . . . | 13        |
| 3.6      | Differential Sensitivity . . . . .                           | 14        |
| 3.7      | Energy Resolution and Energy Dispersion Matrix . . . . .     | 15        |
| 3.8      | Background Rate . . . . .                                    | 16        |
| 3.9      | Uncertainties . . . . .                                      | 18        |
| 3.10     | Comparison with other Instruments . . . . .                  | 19        |
| <b>4</b> | <b>Appendix</b>  | <b>20</b> |
| 4.1      | Description of Analysis Codes: MARS . . . . .                | 20        |
| 4.2      | Description of Analysis Codes: Eventdisplay . . . . .        | 21        |
| 4.3      | Cosmic ray spectra . . . . .                                 | 22        |
|          | <b>Glossary</b>  | <b>25</b> |

# 1 Introduction

This document describes the CTA instrument response functions (IRFs) as provided to the science working groups by the CTA Analysis & Simulation Working group (ASWG). It contains a description of the Monte Carlo simulations and analysis, an explanation of the different performance and sensitivity functions, and technical background on IRF histogram definitions.

**This document describes the CTA IRFs released in Spring 2017.** It will be updated with each release of IRFs.

The text on the IRFs focus on the IRFs files in ROOT format, which are at this point the origin of all IRFs used in CTA (also those in FITS format). For a detailed description of the FITS format and tables, see this [webpage](#)

The intended readership of this report is:

- members of the science working groups using IRFs to simulate the response of CTA to a particular physics model
- developers of high-level analysis tools like ctools or gammapy.
- developers of the instrument response function production pipeline and format for CTA

The IRFs are released by the CTA Analysis & Simulation Working group for internal usage by the consortium members. New IRFs are released when:

- new Monte Carlo (MC) productions with significant updates in the telescope models or array layouts are available
- additional coverage of the parameter space for observation can be provided (e.g. additional zenith angles or levels of night-sky background)
- improved analysis results are available (includes also bug fixes)
- new or additional reconstruction methods or codes have been used

The most up-to-date IRFs from the MC production *prod3b* can be found on the following redmine page:

[https://forge.in2p3.fr/projects/cta\\_analysis-and-simulations/wiki/Prod3b\\_based\\_instrument\\_response\\_functions](https://forge.in2p3.fr/projects/cta_analysis-and-simulations/wiki/Prod3b_based_instrument_response_functions).

This redmine page provides access to a large number of IRFs files and additional plots for both CTA sites and different configurations. A selected subset of the IRFs is also published through the CTA public webpage<sup>1</sup>.

The IRF plots shown in this document are for illustration only; a full set of plots of the provided IRFs are available through the *prod3b* page mentioned in the previous paragraph. .

## 2 Generation of Instrument Response Function for CTA

### 2.1 Monte Carlo Simulations

The performance values are derived from detailed Monte Carlo (MC) simulations of the CTA instrument based on the CORSIKA air shower code and telescope simulation tool *sim\_telarray* [3]. The MC simulations are similar to the one presented in [4] (a very recommended reading), but for an updated detector

---

<sup>1</sup><https://www.cta-observatory.org/science/cta-performance/>

model of the CTA telescopes (so called *production 3b (prod3b)*). Detailed background on the MC production can be found on the corresponding internal websites on the redmine system<sup>2</sup>. Table 1 gives a broad overview of the parameters and number of events in the MC production.

We assume to observe a gamma-ray source with a spectral shape following a power law with  $E^{-2.6}$ . None of the results (e.g. differential flux sensitivities, effective areas, angular or energy resolutions) as presented below depend on the assumed spectral shape of the gamma-ray source (this is in contrast to integral sensitivity, which heavily depends on the assumed spectral index). Background cosmic-ray spectra of proton and electron/positron particle types are assumed using measurements from cosmic-ray instruments, see appendix 4.3 for details. Heavier nuclei like cosmic ray helium are not simulated. Studies from production 1 and 2 show that there is no significant contribution to the residual background from these heavier nuclei; they are much more effectively suppressed by shape cuts. The spectral index assumed in the air shower simulation is generally -2 (Table 1). Events are weighted according to the spectral shapes mentioned above. All air shower simulations make use of the hadronic interaction models QGSJet-II and URQMD above and below 80 GeV respectively.

| particle type                         | spectral index | energy range [TeV] | azimuth angle [deg] | view cone radius [deg] | scatter area [m] | number of uses of each event | total number of events |
|---------------------------------------|----------------|--------------------|---------------------|------------------------|------------------|------------------------------|------------------------|
| <b>Paranal - 20 deg zenith angle</b>  |                |                    |                     |                        |                  |                              |                        |
| gamma (on-axis)                       | -2             | 0.003 - 330        | 0 / 180             | 0                      | 2500             | 10                           | $2 \cdot 10^8$         |
| gamma (diffuse)                       | -2             | 0.003 - 330        | 0 / 180             | 10                     | 3000             | 20                           | $1 \cdot 10^9$         |
| electron                              | -2             | 0.003 - 330        | 0 / 180             | 10                     | 3000             | 20                           | $2 \cdot 10^8$         |
| proton                                | -2             | 0.004 - 600        | 0 / 180             | 10                     | 3000             | 20                           | $8.2 \cdot 10^9$       |
| <b>Paranal - 40 deg zenith angle</b>  |                |                    |                     |                        |                  |                              |                        |
| gamma (on-axis)                       | -2             | 0.006 - 660        | 0 / 180             | 0                      | 2700             | 10                           | $2 \cdot 10^8$         |
| gamma (diffuse)                       | -2             | 0.006 - 660        | 0 / 180             | 10                     | 3300             | 20                           | $1 \cdot 10^9$         |
| electron                              | -2             | 0.006 - 660        | 0 / 180             | 10                     | 3300             | 20                           | $2 \cdot 10^8$         |
| proton                                | -2             | 0.008 - 1200       | 0 / 180             | 10                     | 3300             | 20                           | $8.2 \cdot 10^9$       |
| <b>La Palma - 20 deg zenith angle</b> |                |                    |                     |                        |                  |                              |                        |
| gamma (on-axis)                       | -2             | 0.003 - 330        | 0 / 180             | 0                      | 1400             | 10                           | $2 \cdot 10^8$         |
| gamma (diffuse)                       | -2             | 0.003 - 330        | 0 / 180             | 10                     | 1900             | 20                           | $1 \cdot 10^9$         |
| electron                              | -2             | 0.003 - 330        | 0 / 180             | 10                     | 1900             | 20                           | $2 \cdot 10^8$         |
| proton                                | -2             | 0.004 - 600        | 0 / 180             | 10                     | 1900             | 20                           | $4 \cdot 10^9$         |
| <b>La Palma - 40 deg zenith angle</b> |                |                    |                     |                        |                  |                              |                        |
| gamma (on-axis)                       | -2             | 0.006 - 660        | 0 / 180             | 0                      | 1600             | 10                           | $2 \cdot 10^8$         |
| gamma (diffuse)                       | -2             | 0.006 - 660        | 0 / 180             | 10                     | 2200             | 20                           | $1 \cdot 10^9$         |
| electron                              | -2             | 0.006 - 660        | 0 / 180             | 10                     | 2200             | 20                           | $2 \cdot 10^8$         |
| proton                                | -2             | 0.008 - 1200       | 0 / 180             | 10                     | 2200             | 20                           | $4 \cdot 10^9$         |

**Table 1** – Parameters describing the MC air shower simulations for prod3b.

The performance curves are obtained from two different types of gamma-ray simulations:

**On-axis gamma-ray simulations:** The gamma-ray source is located at the centre of the field of view of each camera.

**Diffuse gamma-ray simulations:** The simulated arrival direction of the primary gamma rays are selected from a cone (diameter 20 deg) around the pointing direction of the telescopes.

Nominal telescope pointing is assumed, with all telescopes pointing directions parallel to each other (performance estimation for other pointing modes, e.g. divergent pointing will be provided in the future). Performance estimations are available for two zenith angles (20° and 40°), and for each zenith angle for two different azimuth angles (corresponding to pointing towards the magnetic North and South). Significant performance differences are found between the two azimuthal pointing directions, especially for the Northern site, as the impact of the geomagnetic field is large enough to influence notably the air shower development.

<sup>2</sup>[https://forge.in2p3.fr/projects/cta\\_analysis-and-simulations/wiki](https://forge.in2p3.fr/projects/cta_analysis-and-simulations/wiki) and [https://forge.in2p3.fr/projects/cta\\_dirac/wiki/CTA-DIRAC\\_MC\\_PROD3\\_Status](https://forge.in2p3.fr/projects/cta_dirac/wiki/CTA-DIRAC_MC_PROD3_Status)

## 2.2 Event Reconstruction and Analysis

The final CTA reconstruction and analysis pipeline is currently under development, and is not available yet for the sensitivity estimations and the IRF productions. Therefore, two fully independent analysis chains based on non-CTA software are currently used:

**MARS Analysis:** The MAGIC Analysis and Reconstruction Software (MARS) is the main analysis software used in the MAGIC collaboration [13]. The MARS analysis for CTA is maintained by the IFAE group.

**Eventdisplay Analysis:** Eventdisplay is one of the official analysis packages of the VERITAS collaboration. The Eventdisplay analysis for CTA is maintained by the DESY group.

The analysis packages have been adapted for the processing of CTA simulations and have been used for the analysis of all CTA large-scale MC productions (prod1, prod2 and prod3). Both analysis chains produce very similar results for sources located at the central part of the field of view (the IRFs obtained are actually interchangeable with negligible impact for almost all physics analyses). For increasing off-axis angles differences between the two analysis chains become notable; at  $\sim 2$  deg and above Eventdisplay outperforms MARS by 30% in the energy range between 100 GeV and a few TeV. Reasons for this are the application of different reconstruction methods and different parameter choices (examples for this are: Eventdisplay uses a modified DISP method for the direction reconstruction, which performance better than the method of intersecting lines for events at large offaxis angles; it also trains the BDTs used for gamma selection in off-axis angle bins, while the MARS reconstruction is training its random forests without binning in off-axis angles).

The software packages perform analyses based on image parameterisations, with different choices of algorithms for image cleaning, background suppression (Boosted Decision Trees vs. Random Forest) and energy reconstruction (Look-up tables in combination with boosted decision trees vs. Random Forest). For a more detailed description of MARS and Eventdisplay, see Appendix 4.1 and 4.2. As both analyses are "classical" ones (based on parametrised shower images), some improvement is expected with the use of more sophisticated techniques fully exploiting pixel-wise information, like e.g. image templates methods [11, 14] (although it is unclear at this point if the relative improvement is similar to what has been observed with the current-generation instruments).

## 2.3 Computing

As explained earlier in this document, instrument response functions are based on full Monte-Carlo simulations starting from the development of air showers in the atmosphere and going through a detailed simulation of the telescope optics and camera electronics. In order to cover the 4 decades in energy, 2 azimuthal pointing directions and 2 zenith angles with a fair statistics in all bins, large amount of computing resources are required, both in term of CPU and disk space. For instance, the IRFs presented in this document, and corresponding to MC prod3 (b), have required the use of around 120 million HS06 CPU hours (1200 CPU years) and about 1.4 PByte of disk storage on the CTA computing grid <sup>3</sup>, since July 2016 as shown in figure 1.

Computing is currently handled on the CTA Computing Grid (CTACG) that gathers resources from more than 20 computing centres across Europe, 6 of which also provide disk and tape storage. Computing centres provide resources on a best effort basis, nevertheless CTA resources end up being quite significant with more than 100 MHS06 CPU hours each year and 2.4 PB of disk storage available. Our Computing Resource Management System (CRMS) is based on the DIRAC framework [6]: CTA can rely on its own DIRAC instance, managed by L. Arrabito (CNRS/IN2P3/LUPM) and that runs on servers spread at 3 computing centres in CC-IN2P3 (Lyon), PIC (Barcelona) and DESY (Zeuthen). DIRAC is also used for data management for now, as all data products are registered in the DIRAC File Catalog with a detailed set of meta data, including the name and version of the software used to produce the files. Besides, the CernVM File System (CVMFS) is used to distribute the software used in production

<sup>3</sup>additional computing power and disk storage was used at some local sites like DESY and MPIK Heidelberg.

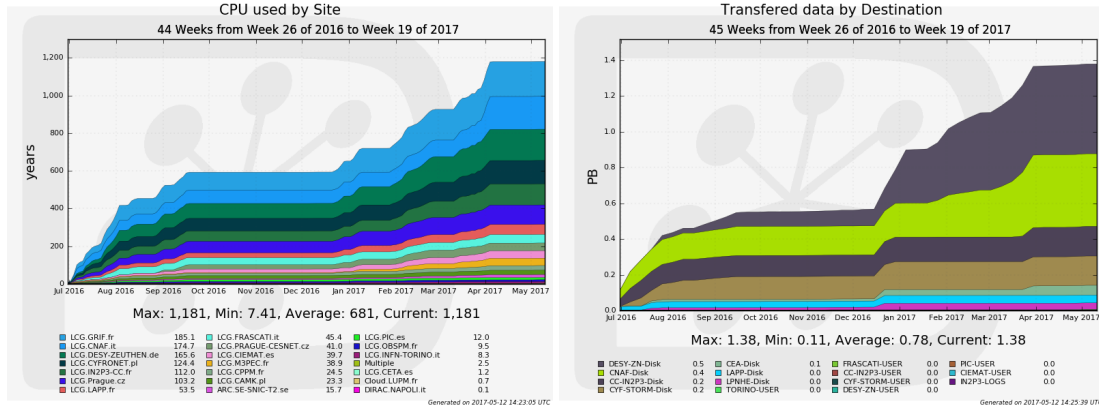


**Figure 1** – Prod 3 (b) computing resources on CTACG. Left, cumulative CPU time. Right, output files written on disk.

across computing sites, and can also be configured by end users on their personal computer if they wish to easily use or explore production software.

The workflow used for production of new simulations is relatively simple, and relies entirely on the DIRAC Transformation System [7] [8]. The first step is to run in a first set of jobs the air shower simulation (CORSIKA) and the instrument response (simtel\_array) for as many telescope/camera positions/associations as needed (still around 300 in prod3 (b)). This is really the hard part that consumes the largest part of the CPU, and requires up to 8 GB of RAM per core and tens of GB of scratch disk for each job. The second step is the calibration, shower analysis and reconstruction and is run in a second set of jobs for both reconstruction software (EventDisplay and MARS): all output products are saved on disk and registered in the file catalogue with meta data, and are hence available for everyone to look into. Then for EventDisplay successive steps are run locally by G. Maier, while for MARS most of the processing is still done on the grid in a sequence of tasks. For both software, the very last step for creating the IRF sets are done by the teams locally.

With prod3 (b) and the beginning of the construction on both sites, the array layout shall be fixed shortly. Further studies of the instrument IRFs shall be done with respect to a reference simulation for each baseline array with fixed telescope/camera associations (unless this is the goal of the study). Simulating just the baseline array will be much more efficient and will allow us to further explore our IRFs in the large phase space of parameters (atmosphere, pointing, NSB, degraded performances, missing telescope...).

## 2.4 Sites and Array Layouts

The CTA sites Paranal (southern site) and La Palma (northern site) are assumed in the configuration of MC prod3b. Table 2 gives an overview of the most important site characteristics. The most notable difference between the two sites is the strength and direction of the geomagnetic field, which has direct implications on CTA sensitivity, angular and energy resolution [9].

For Paranal the assumed array layouts correspond to the final layout HB9 (see discussions and CB at the Kashiwa consortium meeting) and one possible threshold implementation. For La Palma, updated layouts taking into account the restrictions due to the local topography, roads and buildings have been used in the simulations and analysis. The number of telescopes for each layout can be found in table 3 and the layouts can be seen in figure 2. Even if there are still several plausible threshold implementations (see this presentation for the considered scenarios), studies show little performance differences among the most viable possibilities. For now, the implementations HB9-TS-BB and AL4-BN15-TS were chosen.

The decision on the actual telescope and camera types is still pending. The simulations take into account these differences and allow to calculate instrument response functions for all possible combinations of telescopes and camera types. IRFs are available for LSTs, MSTs-NectarCam, MSTs-FlashCam, MST-SCTs, GCTs, SST-1m, and ASTRI type telescopes. Although there are differences in the IRFs of the

different telescope types, the following combinations are provided to the CTA science working group and should be used in general for all physics analyses:

- Southern site (Paranal): LSTs, MST-FlashCam, SST-1m
- Northern site (La Palma): LSTs, MST-NectarCam

For details on the configuration assumed in the MC simulations, see the different reports given at CTA consortium meetings, the [sim\\_telarray prod3 webpage](#), and the Monte Carlo descriptions for each telescope type (see these [reports](#)).

| Site     | Longitude, Latitude<br>[deg] | Altitude<br>[m] | $B_x$<br>[ $\mu$ T] | $B_z$<br>[ $\mu$ T] |
|----------|------------------------------|-----------------|---------------------|---------------------|
| Paranal  | -70.3, 24.07S                | 2150            | 21.4                | -8.9                |
| La Palma | -17.89, 28.76N               | 2147            | 30.8                | 23.2                |

**Table 2** – Site characteristics for the CTA Paranal and La Palma sites.

| Site     | Implementation                    | LSTs | MSTs | SSTs |
|----------|-----------------------------------|------|------|------|
| Paranal  | HB9 (full array)                  | 4    | 25   | 70   |
| Paranal  | HB9-TS (threshold implementation) | 0    | 15   | 50   |
| La Palma | (full array)                      | 4    | 15   | -    |
| La Palma | (threshold implementation)        | 4    | 5    | -    |

**Table 3** – Number of telescopes for each type for each site.



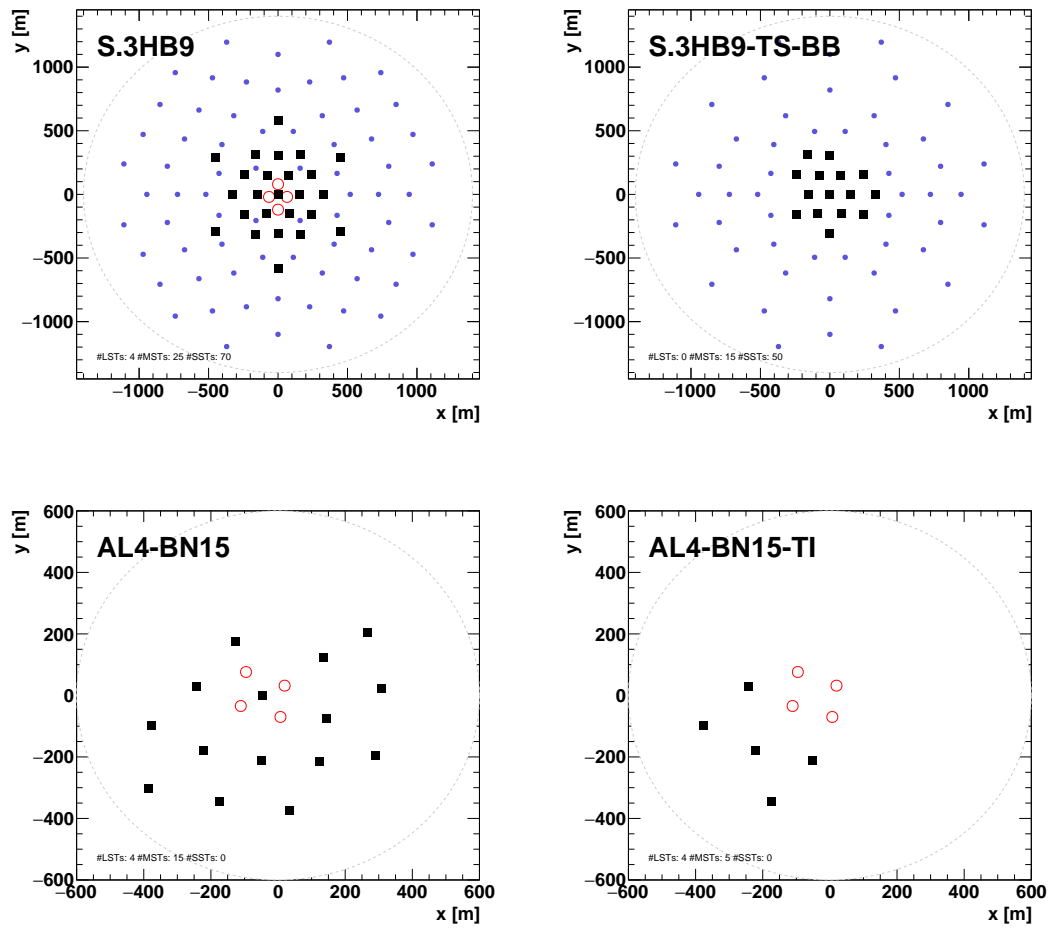


**Figure 2** – Telescope layout for the Southern (top) and Northern site (bottom) for full (left column) and threshold implementation arrays (right column). The open circles indicate LSTs, the filled squares MSTs, and the filled points SSTs (southern site only).

### 3 Description of Instrument Response Functions for CTA

#### 3.1 Definition of variables

We follow the guidelines outlined in "Conventions for CTA dark matter searches (2017)" by J.Rico et al.

- **Energy or True energy** -  $E$  or  $E_T$  - [TeV] - True energy of a gamma ray.
- **Estimated or reconstructed energy** -  $E'$  or  $E_R$  - [TeV] - Estimated energy of a gamma-ray candidate (primary particles like protons or electrons are reconstructed assuming the measured signal is due to gamma rays).
- **[Incoming or true] direction** -  $\bar{p}$  - ([deg],[deg]) - Incoming direction of a gamma ray or in general a point in the sky in camera coordinates, in general relative to the array pointing direction. The vector  $\bar{p}$  connects in the camera plane the FoV centre with the point in the camera which corresponds to the event direction. The array pointing direction is for the nominal pointing mode equivalent to the pointing direction of all telescopes, but different for alternative pointing modes (e.g. the divergent pointing).
- **Estimated [incoming] direction** -  $\bar{p}'$  - ([deg],[deg]) - Reconstructed incoming direction of a gamma-ray candidate in camera coordinates, by default relative to the array pointing direction.
- **Offset angle** -  $\Psi$  - [deg] - Angular distance of the incoming direction of a gamma ray to the pointing direction (calculated in camera coordinates;  $\Psi = |\bar{p}|$ ), useful when radial symmetry around the telescope pointing direction can be assumed.
- **Estimated offset angle** -  $\Psi'$  - [deg] - Angular distance between the estimated incoming direction of a gamma ray and the pointing direction (calculated in camera coordinates;  $\Psi' = |\bar{p}'|$ ).
- **Angular distance to source center** -  $\Theta$  - [deg] - Angular distance between the assumed source center and the reconstructed direction of a gamma ray:  $\Theta = |\bar{p} - \bar{p}'|$  (this is the  $\Theta$  used in the  $\Theta^2$  cut). In the point-source analysis using the diffuse gamma-ray simulation events, the assumed source center is equal to the incoming (true) direction.
- **Observation time** -  $T_{obs}$  [s] - Total effective observation time. System dead time is not taken into account and considered to be negligible<sup>4</sup>.

#### 3.2 General remarks on IRF histograms

- **on-axis** IRFs: the direction of the incoming gamma rays is the same as the telescope pointing direction. The performance of CTA is expected to be rather flat around the centre of the field of view, so these IRFs can be used for sources within the inner  $\sim 1$  degree of the field of view (diameter).
- **off-axis** IRFs: the direction of the incoming gamma rays is at different offset angles  $\Psi$  to the telescope pointing direction. Off-axis angles  $\Psi$  are quoted at bin centres in units of degrees; the off-axis response is calculated from diffuse simulations of gamma-ray primaries and averaged over the given bin width (e.g. the performance at 1.5 deg off-axis angle ( $\Psi = 1.5$  deg) is the average performance in the interval [1 ,2 ] degrees)
- in general all histograms are binned with a 0.2-binning on the logarithmic energy axis (5 bins per decade); some selected histograms (e.g. effective areas or energy migration matrices) are given with a finer binning
- the valid range for the IRFs consists of all energies ( $E_R$  or  $E_T$ ) and offset angles  $\Psi$  for which differential sensitivity values are given. At this point no difference is made among the different causes for an empty bin. One reason might be that CTA is not sensitive at this particular energy;

<sup>4</sup>The CTA performance requirements state a system dead time of  $< 2\%$ .

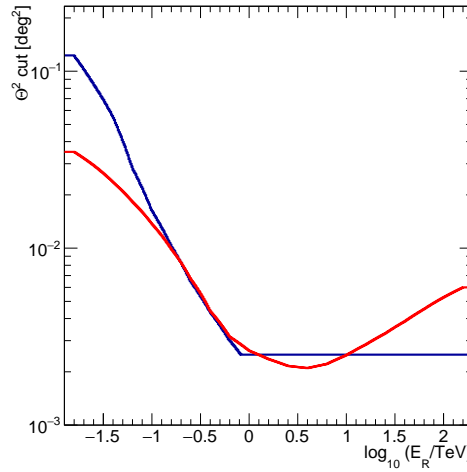


**Figure 3** – Point-source direction cut ( $\Theta^2(E_R)$ -cut) as function of energy for the MARS (red line) and Eventdisplay (black line) analyses. The example shown is for the Paranal site, full array, 20 deg zenith angle, average pointing direction, and 50 h of observation time.

that there are not enough MC statistics (e.g. at the highest energies), that there are no background events left after gamma-selection cuts, or other reconstruction and analysis problems.

All IRFs are provided in ROOT format<sup>5</sup> and are stored as TH1F, TH2F, or TH3F histograms. We note that not all probability distributions are consistently normalised to an integral of one.

### 3.3 Point-source direction ( $\Theta^2$ ) cut

The point-source analysis applied in this performance calculation assumes energy dependent cuts on the incoming direction, often known as  $\Theta^2 = \Theta^2(E_R)$  cuts.

For the eventdisplay analysis,  $\Theta(E_R)$  follows the 68% containment radius of the spatial resolution function with a minimum cut value (typically  $\Theta(E_R)_{min} \geq 0.05 \text{ deg} \forall E_R$ ). In the MARS analysis chain the  $\Theta^2$  cut is part of the sensitivity optimisation procedure. Figure 3 shows an example of the applied cut for both analysis chains.

#### Theta<sup>2</sup>-cut histograms:

- **Theta2Cut:**  $\Theta^2$ -cut as function of reconstructed energy (in  $\text{deg}^2$ )

### 3.4 Collection Area

The **effective collection area** -  $A_{eff}$ : given an area  $A_{tot}$  perpendicular to the pointing axis and sufficiently large so that any gamma ray whose trajectory does not cross  $A_{tot}$  has negligible probability of being detected, then  $A_{eff} = \epsilon \times A_{tot}$  with  $\epsilon$  being the overall detection efficiency for events with trajectory crossing  $A_{tot}$ .

$A_{eff}$  depends on  $E_T$ ,  $\bar{p}$ , the analysis cuts and the observational conditions (zenith and azimuth angle, weather, NSB, etc.).

The effective collection areas for gamma rays are given after gamma-selection cuts, with and without direction ( $\Theta^2$ ) cuts applied.

<sup>5</sup>root.cern.ch

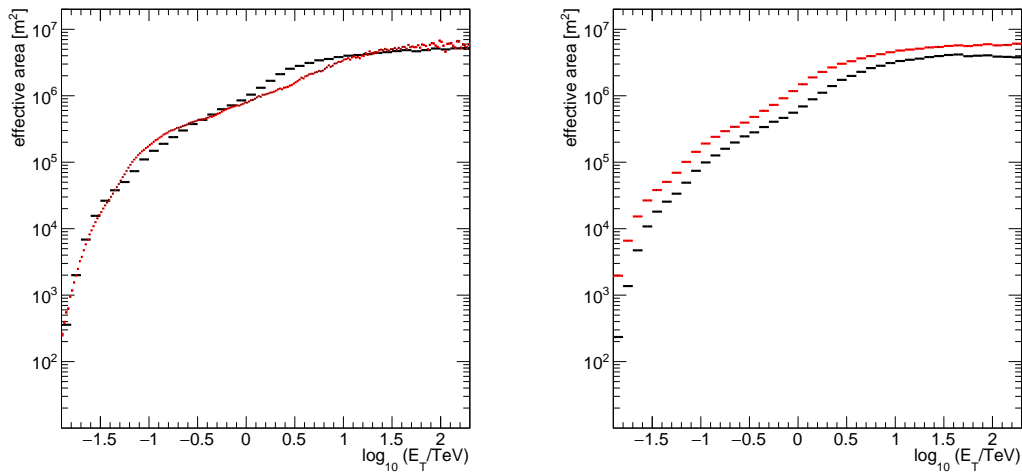


**Figure 4** – Effective collection area as function of true energy  $E_T$ . Left: Effective areas after gamma-selection cuts determined with the MARS (red markers) and Eventdisplay (black marker) analysis chains for the Paranal site, full array, 20 deg zenith angle, average pointing direction, and 50 h of observation time. Right: Effective areas after gamma-selection cuts optimised for observation times of 50 h and 30 min (results shown are from the Eventdisplay analysis chain).

#### Effective collection area histograms:

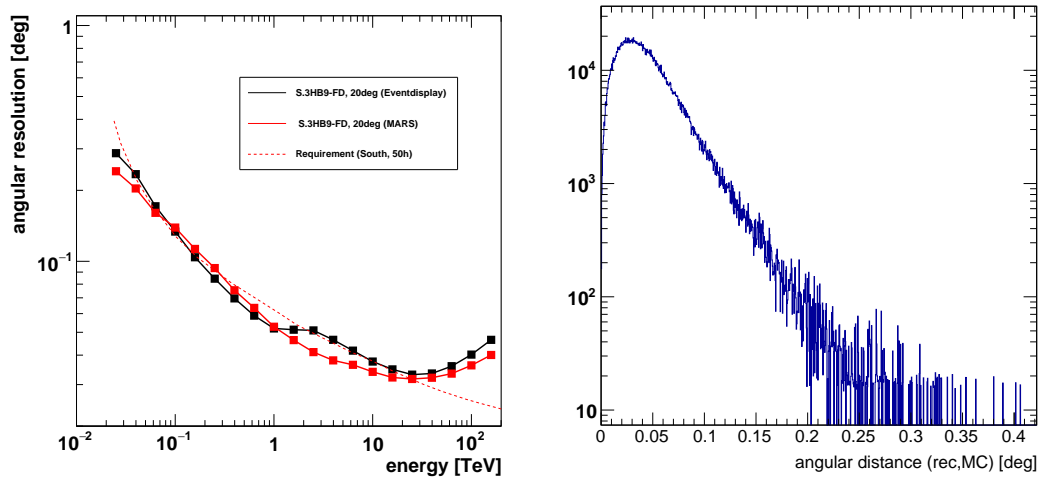
- **EffectiveAreaEtrue:**  $A_{eff}$  as function of true energy  $E_T$  (on axis); direction ( $\Theta^2$ ) cuts applied
- **EffectiveAreaEtrueNoTheta2cut:**  $A_{eff}$  as function of true energy  $E_T$  (on axis); no direction ( $\Theta^2$ ) cuts applied
- **EffectiveAreaEtrue\_offaxis:**  $A_{eff}$  as function of true energy  $E_T$  and off-axis angle  $\Psi$ ; direction ( $\Theta^2$ ) cuts applied
- **EffectiveAreaEtrueNoTheta2cut\_offaxis:**  $A_{eff}$  as function of true energy  $E_T$  and off-axis angle  $\Psi$ ; no direction ( $\Theta^2$ ) cuts applied

Figure 4 shows examples of the effective area described above. Effective areas depend on the gamma-selection cuts. In general, shorter observing times require less restrictive cuts in order to achieve a sufficient number of signal events. Therefore, cuts optimised for shorter observation times produce larger effective areas.

For completeness, effective areas are also provided as function of reconstructed energy  $E_R$ . These are traditionally used in gamma-ray analyses applying the *method of correction factors* instead of un- or forward folding methods which make use of the full information of the energy dispersion matrix. Effective areas as function of reconstructed energy depend on the spectrum assumed in true energy (here: always  $E^{-2.6}$ ).

#### Effective collection area (vs reconstructed energy) histograms:

- **EffectiveArea:**  $A_{eff}$  as function of reconstructed energy  $E_R$  (on axis); direction ( $\Theta^2$ ) cut applied
- **EffectiveAreaNoTheta2cut:**  $A_{eff}$  as function of reconstructed energy  $E_R$  (on axis); no direction ( $\Theta^2$ ) cut applied
- **EffectiveAreaoff\_axis:**  $A_{eff}$  as function of reconstructed energy  $E_R$  and off-axis angle  $\Psi$ ; direction ( $\Theta^2$ ) cut applied
- **EffectiveAreaNoTheta2cut\_offaxis:**  $A_{eff}$  as function of reconstructed energy  $E_R$  and off-axis angle  $\Psi$ ; no direction ( $\Theta^2$ ) cut applied



**Figure 5** – Left: Angular resolution as function of reconstructed energy  $E_R$ . Both curves are calculated for events after gamma-selection cuts and determined with the MARS (red markers) and Eventdisplay (black marker) analysis chains for the Paranal site, full array, 20 deg zenith angle, average pointing direction, and 50 h of observation time. The red-dashed line indicates the required angular resolution for CTA South. Right: Distribution of the angular distance to the assumed source center  $\Theta$  for energies  $E_R$  around 1 TeV (Eventdisplay analysis chain).

### 3.5 Spatial resolution function and angular resolution

The probability distribution (PDF) of the direction estimator  $\vec{p}'$ ,  $D(\vec{p}'|E_T, \vec{p})$ , depends on  $E_T, \vec{p}$ , the analysis cuts and the observational conditions (zenith, weather, NSB, etc.). Under the assumption of radial symmetry around the telescope pointing direction, this becomes:  $D(\Theta|E_T, \vec{p}) = D(|\vec{p}'||E_T, \vec{p})$

The angular resolution is defined as the angle of 68% containment for the angular distance to the assumed source center (Figure 5, left):  $\int_0^{\Theta_{68}} D(\Theta|E_T, \vec{p}) d\Theta = 0.68$ . Gamma-selection cuts are applied before calculating the angular resolution. Note that this analysis is not optimised to provide best angular resolution, but rather best point-source sensitivity, compatible with the minimum required angular resolution. A significantly better angular resolution is possible at the expense of some collection area and sensitivity. For certain cases the tails of  $D$  towards large  $\Theta$  are crucial (e.g. galactic plane survey with the limits due to source confusion); the current analyses are not optimised to minimise the extent of these tails (Figure 5, right).

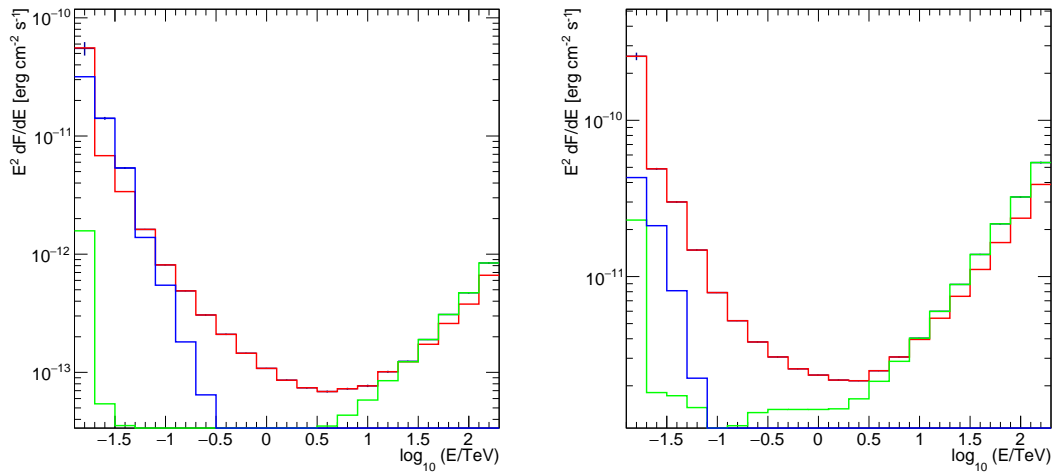


**Figure 6** – Illustration of the restrictive ranges of the three sensitivity requirements for the calculations of different sensitivities vs reconstructed energy  $E_R$  for 50 h (left) and 30 min (right) of observation time (Paranal site, full array, 20 deg zenith angle, average pointing direction, Eventdisplay analysis). The gamma-separation cuts are optimised in both cases to fulfil the three requirements listed in the text. Red lines: differential sensitivity applying the significance requirement only ( $\geq 5\sigma$ ). Green lines: differential sensitivity applying the excess event requirement only (at least 10 excess events). Blue lines: differential sensitivity applying the requirement on systematic limit only (signal excess is at least five times the assumed background systematic uncertainty of 1% of the background remaining after cuts).

#### Angular resolution histograms:

- **AngRes**: Angular resolution (68% containment radius) as function of reconstructed energy  $E_R$  (on axis)
- **AngularPSF2D**: PDF of the direction estimator as function of reconstructed energy  $E_R$  (on axis)
- **AngularPSF2Dtrue**: PDF of the direction estimator as function of true energy  $E_T$  (on axis)
- **AngRes80**: Angular resolution (80% containment radius) as function of reconstructed energy  $E_R$  (on axis; histogram not available in all IRF files)
- **AngRes95**: Angular resolution (95% containment radius) as function of reconstructed energy  $E_R$  (on axis; histogram not available in all IRF files)
- **AngRes\_offaxis**: Angular resolution (68% containment radius) as function of reconstructed energy  $E_R$  and off-axis angle  $\Psi$
- **AngularPSF2D\_offaxis**: PDF of the direction estimator as function of reconstructed energy  $E_R$  and off-axis angle  $\Psi$
- **AngularPSF2Dtrue\_offaxis**: PDF of the direction estimator as function of true energy  $E_T$  and off-axis angle  $\Psi$
- **AngRes80\_offaxis**: Angular resolution (80% containment radius) as function of reconstructed energy  $E_R$  and off-axis angle  $\Psi$  (histogram not available in all IRF files)
- **AngRes95\_offaxis**: Angular resolution (95% containment radius) as function of reconstructed energy  $E_R$  and off-axis angle  $\Psi$  (histogram not available in all IRF files)

## 3.6 Differential Sensitivity

The differential energy flux sensitivity ( $\nu F_\nu$  or  $E^2 \text{ dN/dE}$ ) is calculated in five independent logarithmic bins per decade of energy  $E_R$ . The **required level of confidence in each bin** is a five standard deviation ( $5\sigma$ ) statistical significance (calculated with equation 17 from [12]) and the presence of at least 10 excess events above background. We also require that the signal excess is at least five times the

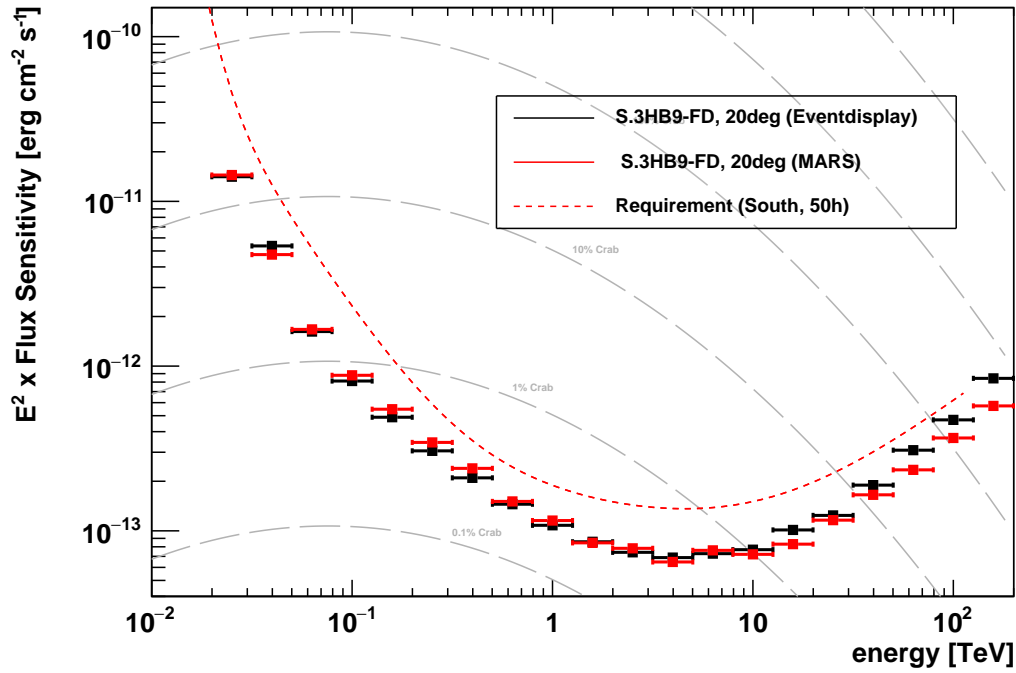


**Figure 7** – Differential sensitivity as function of reconstructed energy  $E_R$  determined with the MARS (red markers) and Eventdisplay (black marker) analysis chains for the Paranal site, full array, 20 deg zenith angle, average pointing direction, and 50 h of observation time. The grey dashed lines indicate the different fractions of the expected flux from the Crab Nebula; the red-dashed line describes the required sensitivity for CTA South.

assumed background systematic uncertainty of 1% of the background remaining after cuts<sup>6</sup>. These requirements are applied for each bin in energy for observations times of 50 h, 5h, 30 min, and 100s. Figure 6 illustrates the impact of these requirements for two different observation times: as expected, the systematic limit is more important for longer observations times and the limits on excess counts is most important for high energies and short observation times.

#### Differential sensitivity histograms:

- **DiffSens:** Differential sensitivity as function of reconstructed energy  $E_R$  (on axis)
- **DiffSens.offaxis:** Differential sensitivity as function of reconstructed energy  $E_R$  and off-axis angle  $\Psi$

### 3.7 Energy Resolution and Energy Dispersion Matrix

The energy resolution is defined such that 68% of gamma rays will have true energy within  $\Delta E$  of their reconstructed energy  $E_R$  (similar to e.g. Figure 67 in [1]). It is derived from the energy dispersion matrix, which is included in the instrument response files. The migration matrix has been smoothed for the public performance curves (not for the IRFs provided for internal usage) to remove tails which were not significant with the available MC statistics. Examples for the CTA energy resolution and migration matrix can be found in Figure 8.

The same remark applies here as for the angular resolution: the energy resolution is determined after gamma-selection cuts, and not for best resolution cuts. A better energy resolution can be obtained with a specialised analysis.

<sup>6</sup>In Eventdisplay, a toy MC is performed calculating the sensitivity from random experiments (Poissonian randomisation of the number excess and background events): the flux sensitivity is defined as the value for which in 50% of the time the sensitivity requirements are fulfilled. Errors are calculated using the  $\pm 34\%$  containment values.

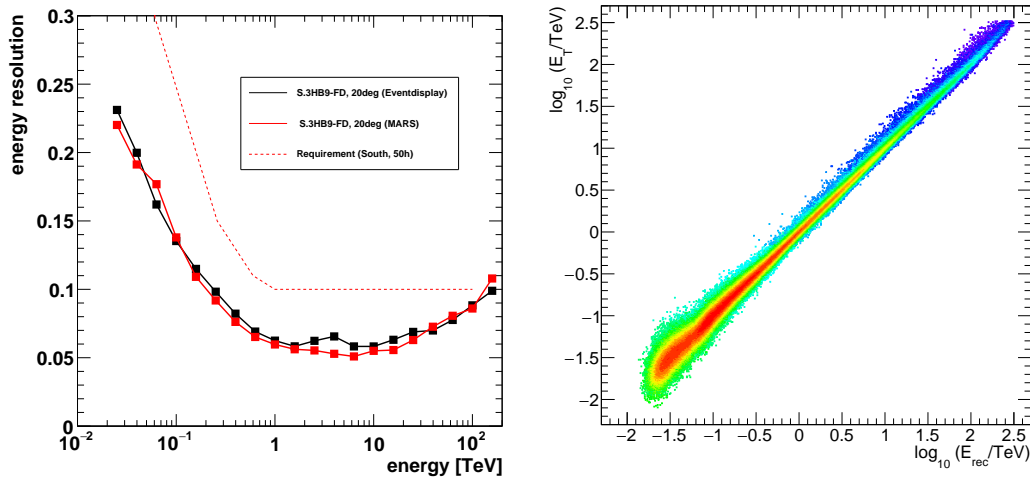


**Figure 8** – Left: Energy resolution as function of reconstructed energy  $E_R$ . Both curves are calculated for events after gamma-selection cuts and determined with the MARS (red markers) and Eventdisplay (black marker) analysis chains for the Paranal site, full array, 20 deg zenith angle, average pointing direction, and 50 h of observation time. The red-dashed line indicates the required energy resolution for CTA. Right: Example for an energy dispersion matrix (Eventdisplay analysis chain).

#### Energy reconstruction histograms:

- **ERes**: Energy resolution as function of reconstructed energy  $E_R$  (on axis); direction ( $\Theta^2$ ) cuts applied
- **MigMatrix**: Energy dispersion matrix (on axis); direction ( $\Theta^2$ ) cuts applied
- **MigMatrixNoTheta2cut**: Energy dispersion matrix (on axis); no direction ( $\Theta^2$ ) cuts applied
- **Ebias**: Energy bias (mean of  $(1 - E_R/E_T)$ -distribution) as function of reconstructed energy  $E_R$  (on axis; histograms not available in all IRF files); direction ( $\Theta^2$ ) cuts applied
- **EestOverEtrue**: Distribution of  $E_R/E_T$  as function of true energy  $E_T$  (on axis); direction ( $\Theta^2$ ) cuts applied
- **ERes\_offaxis**: Energy resolution as function of reconstructed energy  $E_R$  and off-axis angle  $\Psi$ ; direction ( $\Theta^2$ ) cuts applied
- **MigMatrix\_offaxis**: Energy dispersion matrix as function of off-axis angle  $\Psi$ ; direction ( $\Theta^2$ ) cuts applied
- **MigMatrixNoTheta2cut\_offaxis**: Energy dispersion matrix as function of off-axis angle  $\Psi$ ; no direction ( $\Theta^2$ ) cuts applied
- **Ebias\_offaxis**: Energy bias (mean of  $(1 - E_R/E_T)$ -distribution) as function of reconstructed energy  $E_R$  and off-axis angle  $\Psi$  (histograms not available in all IRF files); direction ( $\Theta^2$ ) cuts applied
- **EestOverEtrue\_offaxis**: Distribution of  $E_R/E_T$  as function of true energy  $E_T$  and off-axis angle  $\Psi$ ; direction ( $\Theta^2$ ) cuts applied

Note that all information on the energy reconstruction is available through the energy dispersion matrix; all other histograms (like energy resolution or bias) are derived from these matrixes.

## 3.8 Background Rate

The residual cosmic-ray background rate vs reconstructed gamma-ray energy  $E_R$  is calculated using simulated proton and electron events. The rate is the one integrated in 0.2-decade-wide bins in re-



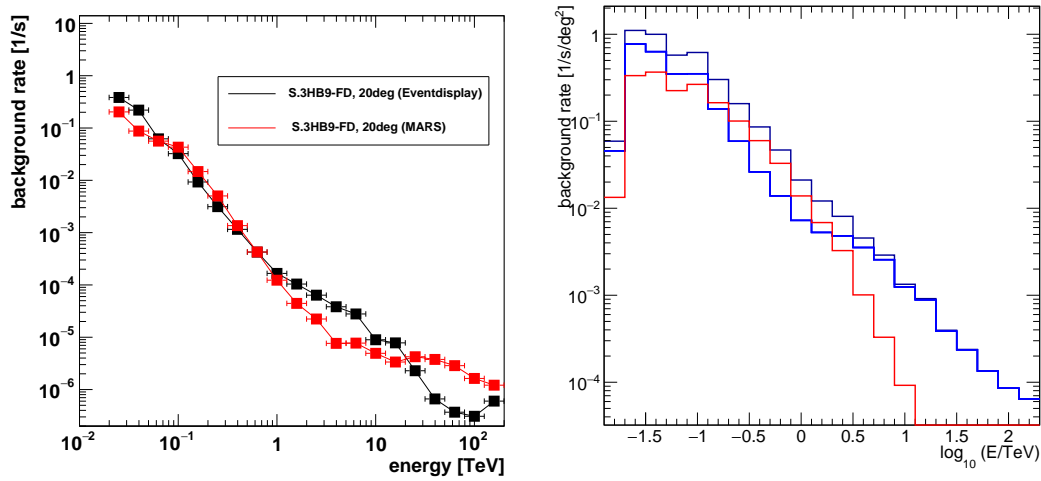


**Figure 9** – Left: Background rate as function of reconstructed gamma-ray energy  $E_R$  for events after gamma-selection cuts and determined with the MARS (red markers) and Eventdisplay (black marker) analysis chains for the Paranal site, full array, 20 deg zenith angle, average pointing direction, and 50 h of observation time. The differences in the results between the two analysis chains are a result of the different gamma-selection cut optimisation methods. Right: Background rates per solid angle as a function of reconstructed energy  $E_R$  (Eventdisplay analysis chain). Black line: combined electron plus proton rate. Red line: electron background only. Blue line: proton background only.

constructed energy  $E_R$  (i.e. five bins per decade). The arrival directions of the primary protons and electrons are selected from a cone around the pointing directions of the telescopes. Background rates are calculated as average background in rings around the pointing directions (width given by the binning in off-axis angle; e.g. for an off-axis angle of 1.5 deg, the ring width is 1 deg). The size of these rings is used to normalise the IRFs given per solid angle.

Gamma-selection cuts optimised for different observing times are applied to the selection of simulated cosmic-ray proton and electron events; a cut on arrival direction, optimised (energy-wise) for best sensitivity to point-like gamma-ray sources, was also applied. For details on the assumed cosmic-ray proton and electron spectra, see appendix 4.3 and [4].

The residual cosmic-ray background rate vs reconstructed gamma-ray energy  $E_R$  is shown in Figure 9 (left) for 50 h-optimised cuts. This, together with the angular resolution and the gamma-ray collection area without angular cut, can be used to simulate the CTA performance to moderately extended sources in the central part of its FoV. The contribution of protons and electrons to the total rate of background events is shown in Figure 9 (right). The plot shows that CTA is able to suppress background events due to primary protons well below the electron background in the range from 200 GeV to several TeV. Events from primary electrons appear very similar to gamma events for CTA and are much harder to suppress than proton events.

**Background rate histograms:**

- **BGRate**: background rate as a function of reconstructed energy  $E_R$  (on axis; integrated rate per energy bin)
- **BGRatePerSqDeg**: background rate per solid angle as a function of reconstructed energy  $E_R$  (on axis)
- **ProtRate, ElecRate**: proton/electron background rate as a function of reconstructed energy  $E_R$  (on axis; integrated rate per energy bin)
- **BGRate\_offaxis**: background rate as a function of reconstructed energy  $E_R$  and off-axis angle  $\Psi$  (integrated rate per energy bin)
- **BGRatePerSqDeg\_offaxis**: background rate per solid angle as a function of reconstructed energy  $E_R$  and off-axis angle  $\Psi$
- **ProtRate\_offaxis, ElecRate\_offaxis**: proton/electron background rate as a function of reconstructed energy  $E_R$  and off-axis angle  $\Psi$  (integrated rate per energy bin)

### 3.9 Uncertainties

The IRFs for CTA are derived from Monte Carlo simulations and reflect our best knowledge of the measurement process and of the instrument at the time of the production of the Monte Carlo. However, there are notable systematic uncertainties on the different performance curves, the most important ones are listed below. We cannot give at this point a good estimation of the impact of each of these uncertainties; this requires dedicated studies which are planned for the future.

Sources of systematic uncertainties (incomplete list):

**MC Model of the CTA telescopes:** The Monte Carlo model is the complete set of parameters which determines the shower, atmospheric, and detector models used in a MC production. The current MC model of the CTA telescopes is based on discussions between the MC group and the instrument teams that date back to 2015. The technical implementation changed for some systems since then, and new measurements and better characterisation of the different parts of the telescopes by the instrument teams will lead in the future to improved MC calculations and more realistic models. It is difficult to quote a number of the expected uncertainty from the differences between the current MC model and the actual implementation of CTA – we expect it to be smaller than the differences between the predictions of production 2 and 3 (at most energies less than 30% in differential flux sensitivity).

**Air-shower simulations:** Air-shower simulations depend on the correct modelling of the hadronic interactions, with uncertainties due to limitations of accelerator-based measurement. CTA suppresses a large fraction of the simulated background events; results are especially sensitive to pion production rates.

**Atmosphere:** Variations in the atmosphere – important for the production and losses of Cherenkov light – are ignored in the derivation of the IRFs.

**Reconstruction methods:** The calibration, reconstruction, and analysis methods used for the determination of the IRFs are based on software chains developed for current generation gamma-ray observatories. Some of the methods applied might introduce systematic errors (e.g. a shift in reconstructed direction as a function of core position), which are not known at this point.

**Cosmic-ray spectra:** The calculation of the number of background events depend on the parameterisation of the cosmic-ray proton and electron spectra from the available data from space- and ground-based observatories. Appendix 4.3 (especially Figure 12 for the parameterisation of the cosmic electron spectrum) and the literature give an indication on the uncertainties.

**Statistical uncertainties due to the limited number of simulated events:** The number of simulated events is limited and especially barely sufficient at the highest energies. Air-shower events are

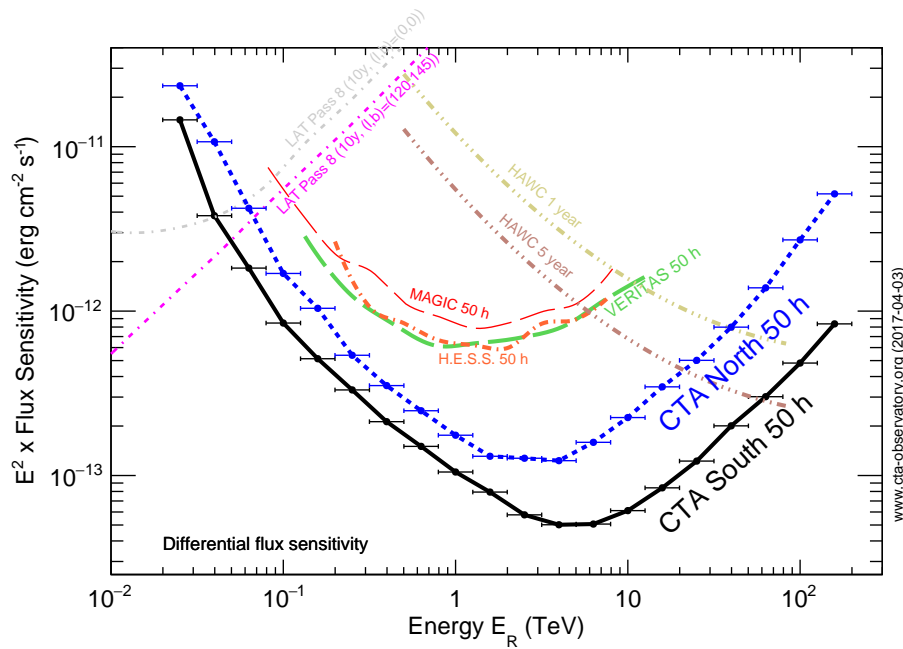


**Figure 10** – Differential sensitivity of CTA in comparison with currently operating ground- and space-based gamma-ray observatories (derived from the analysis of prod2 simulations).

also used several times (see Table 1), which makes it difficult to calculate in all cases statistical uncertainties.

### 3.10 Comparison with other Instruments

The comparison of performance curves provided by different collaborations is by far not straight forward. Different definitions of what sensitivity means, different bin sizes, containment radii, etc make the comparison very difficult. Please take this into account when discussing the curves provided on the public web page (see also Figures 10 and 11). The sensitivity curves are provided by the different collaborations through publications, web pages, or private communication (see [public web page](#) for references).

Note that all figures discussed in this chapter are from the CTA public performance page and the result of the analysis of production 2 simulations.

Known caveats:

- differential sensitivity for HAWC and the Fermi LAT are given in 4 bins per decade. The curves for Fermi-LAT and HAWC are therefore scaled by a factor 1.2 to account for the different energy binning.
- the detection technique of HAWC is very different to CTA and their requirements for a detection per bin are also different (e.g. no requirement on the excess event number)
- angular and energy resolution differ significantly between the instrument (e.g. for HAWC, the energy resolution is larger than the bin size of the differential sensitivity curves)
- angular resolution for HAWC: the curve called optimal bin has been used, which is according to HAWC experts close to 68% containment (the other curve is the 1 sigma of a 2D Gaussian)
- the sensitivity definition is very similar between CTA and Fermi LAT (likelihood ratio test statistic of 25 and at least 10 photons.). The main difference for CTA is the requirement on the systematic uncertainty on the residual background estimation.

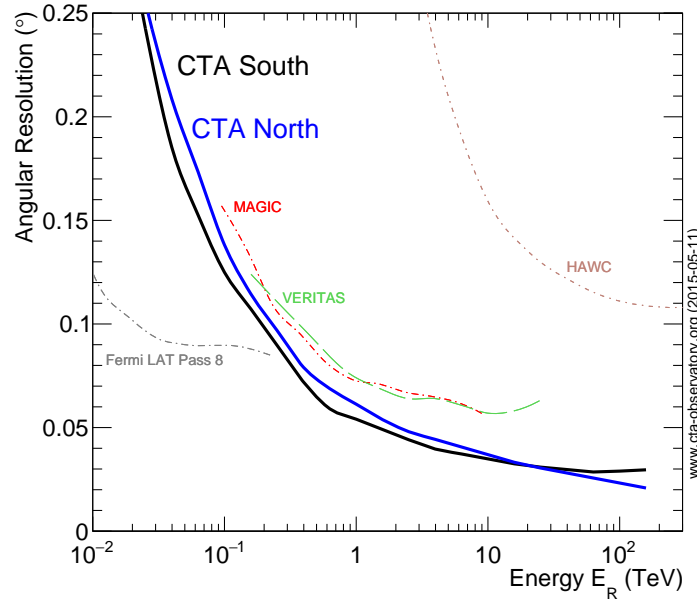


**Figure 11** – Angular resolution of CTA in comparison with currently operating ground- and space-based gamma-ray observatories (derived from the analysis of prod2 simulations).

## 4 Appendix

### 4.1 Description of Analysis Codes: MARS

MARS (MAGIC Analysis and Reconstruction Software [13, 17]) is the official analysis package for the analysis of the MAGIC data. In 2008 MARS was adapted to allow the processing of CTA simulations produced by `sim_telarray`, starting from the Prod-1 library. The analysis of the various CTA Monte Carlo libraries with MARS has been presented in many CTA consortium meetings, starting from the one held in Cracow in 2009. The MARS analysis of the Prod-2 MC was also used to obtain the expected CTA performance that was publicly released on May 2015 <sup>7</sup>.

Although the MAGIC and CTA analyses share the framework and many algorithms, some parts of the chain were specifically developed for CTA. The process starts with the conversion of the `sim_telarray` output into a ROOT-based[15] format, with a program dubbed `chimp`. `Chimp` performs a peak search on the FADC traces of all pixels and then uses those with significant signals to determine the Volume Of Interest (in space (x,y) and time) on each camera. Next, a second pass is carried out on non-significant pixels, integrating their traces around the expected arrival time of Cherenkov photons. The peak-search and integration windows are adapted to the width of the pulses in each camera type. For the FlashCam cameras a digital filter algorithm provided by the FlashCam team is applied to the raw pulses before the trace integration process, to improve the signal to noise ratio. The calibration into absolute (p.e.) units relies on the calibration constants provided by `sim_telarray`. Finally, `chimp` writes out the pixel data (integrated charge and time of peak) for subsequent analysis with MARS. The next steps of the chain are the following:

1. Image cleaning: a simple two-level image cleaning (core and boundary pixels) is applied to select pixels which likely collected Cherenkov photons. Boundary pixels are required to have at least one core neighbour. The boundary threshold is (somewhat arbitrarily) fixed to half the core threshold, and both are then tuned for each camera type to a level such that no hint of the pure-NSB branch is seen in the post-cleaning single pixel spectrum.
2. Image parametrisation: classical Hillas parameters [10] are calculated on the cleaned image, together with the so-called image concentration (fraction of total light recorded in the two brightest

<sup>7</sup><https://www.cta-observatory.org/science/cta-performance/>

pixels).

3. Stereoscopic reconstruction: images with more than 50 p.e. and whose centre of gravity (weighted average mean position of all image pixels after image cleaning) lies within 80% of the nominal camera radius are selected for stereoscopic reconstruction of the shower geometry. A maximum likelihood fit is performed to obtain the shower axis parameters (direction, core location). In this fit each image takes part with a weight calculated according to its elongation (Width/Length) and Size (total light content).
4. Energy reconstruction: a Random Forest (RF) algorithm (a custom implementation available in MARS [2]) is used to estimate the energy. The input parameters are both image parameters (Size, Width, Length, Concentration) and stereo-reconstructed parameters (impact parameter, height of shower maximum). The position of the image on the camera is also used, since it correlates to the viewing angle (from a given telescope) relative to the magnetic field - and hence to the expected Cherenkov light density on the ground. The Random Forest is grown (trained) for each telescope type using an independent gamma MC sample. For any given event, each individual triggered telescope obtains its own estimate (with uncertainty) of the energy, and a weighted average is made to obtain the final estimated energy. An a posteriori check of the correlation of true vs. estimated energy is made, to remove in as much as possible any possible energy reconstruction bias.
5. Particle identification: similar to energy reconstruction, a telescope-wise RF is used with similar input parameters Width, Length, Size, Concentration, impact parameter and height of shower maximum, plus the energy reconstructed by the given telescope, and the global reconstructed energy. These random forests are trained for each telescope type using a sample of MC gammas and protons. During shower reconstruction each telescope produces a value for the so-called Hadronness (the RF output), a parameter which ranges from 0 (very gamma-like image) to 1 (very hadron-like image). Since the particle identification capabilities increase with the brightness of the image, a global hadronness is calculated through an average of all the individual values, weighted with a function of the image Size (which is currently just the square root of the Size parameter - a weight determined empirically from the first CTA MC production).

After the above steps, we have a few basic (estimated) parameters per event, the most relevant of which are the reconstructed direction and energy, the Hadronness, and the telescope multiplicity. The data are then binned in reconstructed energy (in 0.2-dex bins). In each energy bin, cuts in multiplicity (scanned from  $\geq 2$  to  $\geq 9$  telescopes of any type), Hadronness (from 0.5 to 0.95 gamma efficiency) and event direction (from 0.5 to 0.95 gamma efficiency) are optimized in order to achieve the best possible (point-like-source) gamma-ray flux sensitivity (against the background of cosmic-ray electrons and protons), according to the standard definition within CTA ( $5\sigma$ ,  $\geq 10$  events,  $\geq 5\%$  of residual background).

## 4.2 Description of Analysis Codes: Eventdisplay

Eventdisplay is one of the main software packages developed for the analysis of data and simulations in the VERITAS collaboration. It has been adapted for the analysis of CTA MC simulations for all productions (prod1-3). Results obtained with Eventdisplay have been presented at several consortium meetings (e.g. in Liverpool, Munich, Warsaw). The code is public and available to all members of the CTA consortium [5]. A detailed description of the analysis steps and the most important algorithms can be found elsewhere [5]. We describe below the most important analysis stages and concentrate then on the steps related to optimisation. Sensitivities are calculated for point-sources only; extended sources or diffuse gamma-ray emission is beyond the scope of this work.

Eventdisplay is a full reconstruction pipeline. The steps relevant for the analysis of CTA Monte Carlo simulations are:

1. conversion from sim telarray (hessio/eventio) format to Eventdisplay DST format and determination of calibration parameters

2. calibration and FADC trace integration, image cleaning, image parameterisation [10] direction and core reconstruction
3. training and use of lookup tables to estimate the energy and the main gamma-selection parameters mean scaled width and mean scaled length
4. training of boosted decision trees (using the TMVA implementation) in seven different energy bins
5. calculation of effective areas, angular and energy resolution
6. calculation of sensitivities and writing of PHYS performance files (in ROOT format)

The main challenge for the Prod3 array layout analysis is to find analysis parameters which provide good performance for the many different array layouts, and the six different telescope/camera design (LST, FlashCam, NectarCam, GCT, SST-1M, ASTRI). It should be clear that it was impossible to find the absolutely best parameters, given their large number and the variety of array layouts. Many checks have been done to eliminate the impact of the parameter choice.

The following steps have been chosen to obtain robust results:

1. loose low-level quality cuts are chosen by looking at a large number of events for different array layouts: the typical cuts are a minimum number of pixels per image ( $> 4$ ), a minimum number of telescopes (the minimum multiplicity is fixed throughout the analysis to two), for two telescope events the minimum angle between the image axes ( $> 15$  deg), a maximum uncertainty in the energy and direction reconstruction, and a cut removing images which are cut off at the edge of the camera field of view.
2. the cut on the photon direction is energy dependent and follows the angular resolution curve (68% containment radius).
3. the optimal gamma/hadron separation cut is selected on the outcome of the boosted decision trees at the value giving highest detection significance (using the Li & Ma equation 17 to calculate significances), assuming a Crab Nebula-like gamma-ray spectrum and proton+electron background spectrum. The optimal BDT cut values depend on the observation time assumed and is determined for each energy bin considered.
4. the maximum signal efficiency is set to 80%. This is especially important at high energies, where statistics for the BDT training are low and gives robustness against statistical fluctuations.

The minimum telescope multiplicity for each event is not automatically optimised in the Eventdisplay analysis, but a fixed parameter set to a minimum multiplicity of three (for 30 min and 100 s exposures) or four (for 5 h and 50 h exposures). This allows to keep a large fraction of the signal events in the analysis and obtain relatively smooth effective area curves. However, in comparison to an analysis with higher (or bin-wise optimised) multiplicity cuts (e.g. the MARS analysis) or to an Eventdisplay analysis with a fixed multiplicity of four this leads to an increased background rate.

## 4.3 Cosmic ray spectra

### 4.3.1 Proton spectrum

The cosmic proton spectrum is parameterised by the following power-law function:

$$\frac{dN}{dE} = I_0 \left( \frac{E}{E_c} \right)^{-\Gamma}$$

with  $I_0 = 9.8 \times 10^{-6} \text{ cm}^{-2} \text{ s}^{-1} \text{ TeV}^{-1}$ ,  $E_c = 1 \text{ TeV}$ , and  $\Gamma = 2.62$ .

(from a fit to ATIC results)

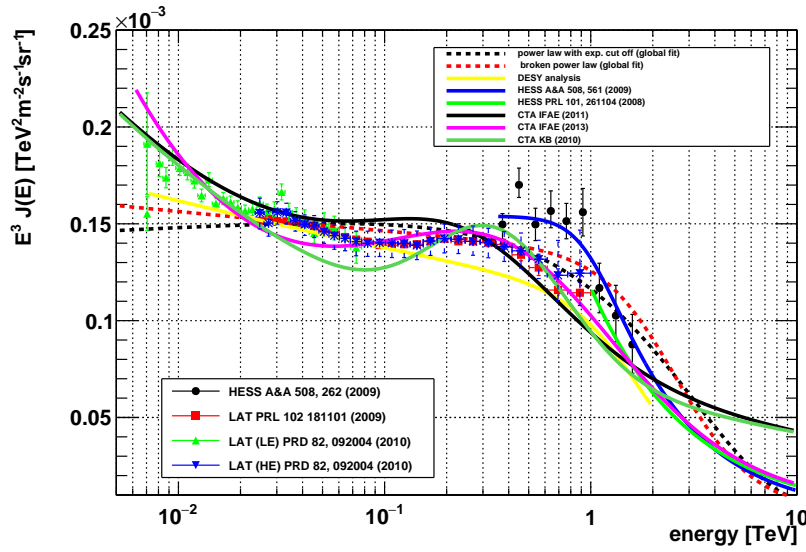


**Figure 12** – Differential energy spectrum of cosmic-ray electrons measured by different observatories. For the CTA analysis, the spectral fit labeled 'IFAE 2013' is used (purple line).

### 4.3.2 Electron spectrum

The cosmic electron spectrum is parameterised assuming the following function (see purple line in Figure 12):

$$E^3 \frac{dN}{dE} = I_0 \left( \frac{E}{E_c} \right)^{-\Gamma} * (1 + f \times (\exp(\text{Gauss}(\log(E/E_c), \mu, \sigma)) - 1))$$

with  $I_0 = 2.385 \times 10^{-9} \text{ cm}^{-2} \text{ s}^{-1} \text{ TeV}^{-1}$ ,  $E_c = 1 \text{ TeV}$ ,  $\Gamma = 3.43$ ,  $\mu = -0.101$ ,  $\sigma = 0.741$ , and  $f = 1.950$ .

## References

- [1] Ackermann, M. et al (The Fermi LAT Collaboration) 2012, *ApJS*, 203, 70
- [2] Albert J., Aliu E., Anderhub H. et al. (2008). Implementation of the Random Forest method for the Imaging Atmospheric Cherenkov Telescope MAGIC. *Nuclear Instruments and Methods in Physics Research A*, 588, 424
- [3] Bernlöhner, K. 2008, *Astroparticle Physics*, 30, 149
- [4] Bernlöhner, K. et al (The CTA Consortium) 2013, *Astroparticle Physics*, 43, 171
- [5] eventdisp webpage: <https://znwiki3.ifh.de/CTA/Eventdisplay%20Software>
- [6] DIRAC (Distributed Infrastructure with Remote Agent Control): <http://diracgrid.org/>
- [7] Arrabito, L. et al, *Prototype of a production system for Cherenkov Telescope Array with DIRAC*, 2015 CHEP Proceedings, <http://iopscience.iop.org/article/10.1088/1742-6596/664/3/032001/pdf>
- [8] Arrabito, L. et al, *The Cherenkov Telescope Array production system for Monte Carlo simulations and analysis*, 2016 CHEP Proceedings, to be published
- [9] Hassan, T. et al, *Monte Carlo Performance Studies for the Site Selection of the Cherenkov Telescope Array*, *Astroparticle Physics*, 2017, ISSN 0927-6505



- [10] A.M. Hillas, in: Proc. 19th ICRC, vol. 3, 1985, p. 445.
- [11] Le Bohec, S. and others 1998, NIM A 415, 425
- [12] Li, T.P. & Ma, Y.Q. 1983, ApJ, 272, 317
- [13] Moralejo, A., Gaug M., Carmona E. et al. (2009). MARS, the MAGIC Analysis and Reconstruction Software. arXiv:0907.0943
- [14] Parsons R.D. & Hinton J.A. (2014). A Monte Carlo template based analysis for air-Cherenkov arrays. Astroparticle Physics, 56, 26
- [15] ROOT webpage: <http://root.cern.ch/>
- [16] Shayduk, M. et al 2013 arXiv-1307.4939
- [17] Zanin, R. et al 2013 ICRC Proceedings <http://www.cbpf.br/~icrc2013/papers/icrc2013-0773.pdf>



## Glossary

ASWG Analysis & Simulations Working Group

CTA Cherenkov Telescope Array

FOV Field of View

IRF Instrument Response Function

MC Monte Carlo